Mon. Not. R. Astron. Soc. **323**, 402–416 (2001)

Close stellar encounters with planetesimal discs: the dynamics of asymmetry in the β Pictoris system

J. D. Larwood[1]★ and P. G. Kalas[2]★

[1]*Astronomy Unit, Queen Mary & Westfield College, Mile End Road, London E1 4NS*
[2]*Astronomy Department, University of California, 601 Campbell Hall, Berkeley, CA 94709, USA*

Accepted 2000 November 9. Received 2000 November 7; in original form 2000 August 7

ABSTRACT

We numerically investigate the dynamics of how a close stellar fly-by encounter of a symmetrical circumstellar planetesimal disc can give rise to the many kinds of asymmetries and substructures attributed to the edge-on dusty disc of β Pictoris. In addition we present new optical coronagraphic observations of the outer parts of the disc of β Pic, and report that the radial extent is significantly greater than was found in previous measurements. The north-easterly extension of the disc's mid-plane is now measured out to 1835 au from the star; the south-westerly component is measured out to 1450 au. Thus the asymmetry in the length of the former with respect to the latter is approximately 25 per cent. We proceed to use the length asymmetry induced in the distribution of simulation test particles as the principal diagnostic feature when modelling the disc response in order to constrain fly-by parameters. In particular we favour a low-inclination prograde and near-parabolic orbit perturber of mass approximately $0.5\,M_{\odot}$. These initial conditions suggest that the perturber could have been physically associated with β Pic prior to the encounter. Thus we also consider the possibility that the perturber could be bound to β Pic, a consideration also of general interest where dust discs are known to exist in binary star systems. We show that a further consequence of a low-velocity encounter is that the perturber could have captured planetesimals from the β Pic disc, and we deduce that as a result of this the perturber could display a dust disc that is presently amenable to observation. In some of our models, we can relate groupings of perturbed particles to the large-scale structure of the β Pic disc. The groupings correspond to high-eccentricity and high-inclination particles that reach apocentre and maximum height in the south-west, moderately eccentric and low-inclination particles that reach apocentre in the north-east, and relatively unperturbed particles inside $\sim$200 au radius.

Key words: stellar dynamics – celestial mechanics – circumstellar matter – stars: individual: β Pic – planetary systems.

1 INTRODUCTION

The starlight of β Pic scatters off dust grains in its edge-on circumstellar disc (Smith & Terrile 1984). Optical imaging reveals that the disc exhibits asymmetrical structure with respect to an ideal disc on projected radial scales from $\sim$50 au (Burrows, Krist & Stapelfeldt 1995; Mouillet et al. 1997) to $\sim$1000 au (Smith & Terrile 1987; Kalas & Jewitt 1995). Kalas & Jewitt (1995) presented sensitive *R*-band images that showed that the north-east (NE) extension could be detected out to 790 au, whereas the south-west (SW) extension was detectable out to just 650 au, corresponding to a $\sim$20 per cent length asymmetry. More recently, the longer NE mid-plane extension has been discovered to carry several brightness enhancements from $\sim$500 to 800 au (Kalas et al. 2000, hereafter KLSS), which have been attributed to a series of rings within the mid-plane of the disc. Similar features in the SW extension were not detected and so eccentric rings were hypothesized.

KLSS presented a dynamical model in which the stellar fly-by scenario (Kalas & Jewitt 1995) for generating the disc asymmetries was applied to the β Pic system. Their finding was that the asymmetry types present in the β Pic disc have analogues in the dynamical response of a particle disc to a perturbing stellar fly-by encounter. Furthermore, they demonstrated that these features could occur simultaneously with the formation of eccentric circumstellar rings. A simple analysis of the perturbed

★ E-mail: j.d.larwood@qmw.ac.uk (JDL); kalas@astron.berkeley.edu (PGK)

disc model was found to be in good quantitative agreement with the observations of both β Pic's disc asymmetries and the mid-plane features, for particular values of the viewing angle and epoch, and fly-by parameters. In this paper we present new observations and measurements of the length asymmetry of the scattered-light disc of β Pic, and then go on to simulate the dynamics of a stellar fly-by encounter with an initially symmetrical disc of particles.

Similar numerical modelling to that presented here and in KLSS has been considered previously in the context of angular momentum transfer between the perturber's orbit and a proto-stellar disc (Clarke & Pringle 1993; Hall, Clarke & Pringle 1996), the dynamics of the Edgeworth–Kuiper belt (Ida, Larwood & Burkert 2000), and the tidal interaction of spiral galaxies (Toomre & Toomre 1972). Here we shall consider a wider range of encounter velocities (from bound orbits through to hyperbolic trajectories) and stellar masses (from M dwarfs to A stars, when scaled to the mass of β Pic) than has been studied before in any context. We also include a discussion of the orbital dynamics of captured particles with respect to the perturber. This paper can be considered as a companion to KLSS since here we also supplement their finding of circumstellar ring formation in similar simulations with an explanation of the dynamical origin of the features.

As in other works (Whitmire, Matese & Tomley 1988; Mouillet et al. 1997; KLSS) we assume that the distribution of the simulation particles represents the distribution of an underlying disc of planetesimals, which are parent bodies whose infrequent and therefore dynamically inconsequential collisions supply the dust scattering surface that is observed in the real system. A more complete model should include consideration of grain removal and generation processes in determining the appearance of the perturbed disc (reviewed by Backman & Paresce 1993). However, we defer treatment of those issues to future work, and focus here on the first-stage problem of the dynamics. This stage is important in deducing the mass and orbital parameters of the postulated stellar perturber, for which it is possible to perform star catalogue searches (e.g. Kalas, Deltorn & Larwood 2001), and we proceed to do this by examining the length asymmetry, and other measures of the disc response, as a function of stellar encounter parameters. However, we choose to examine the length asymmetry as the principal diagnostic measure of the disc response since it is the most distinct such feature both in the observations and in the dynamical models. In our future work we shall also consider the subtler asymmetries in greater detail.

In Section 2 we present deep optical coronagraphic images of the disc. In Section 3 we describe the results of our numerical

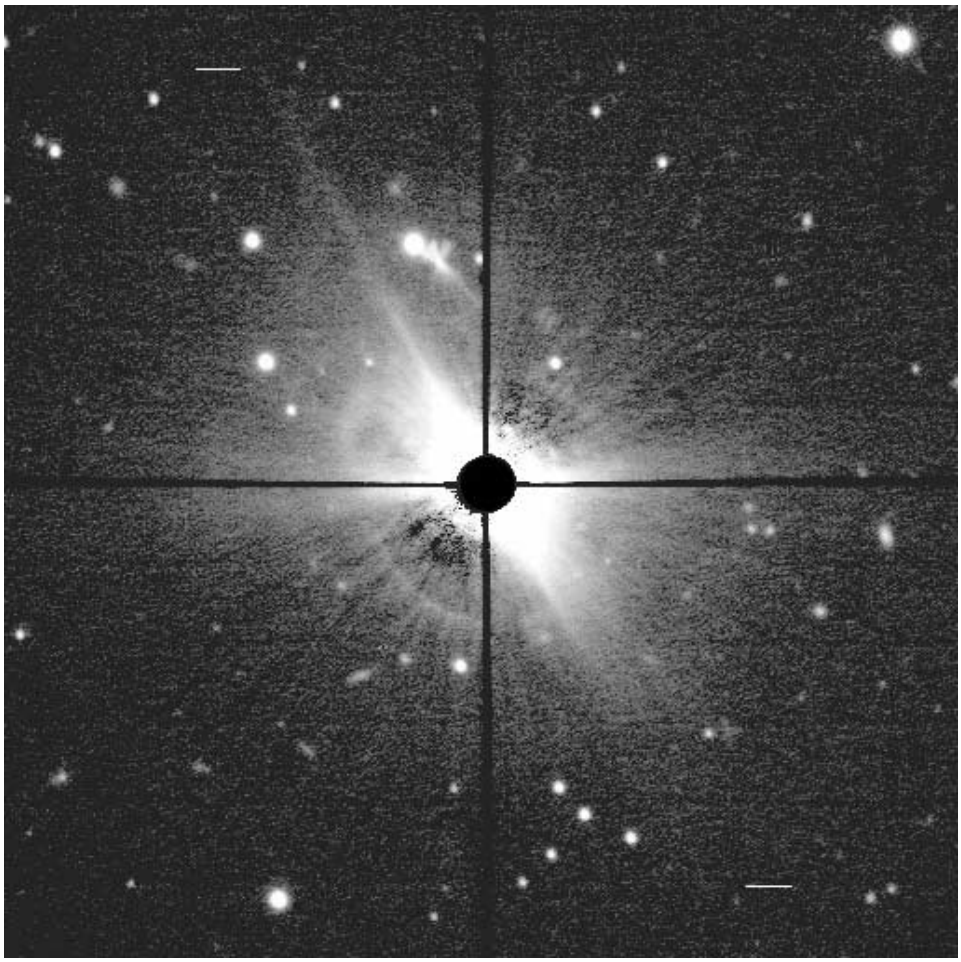

Figure 1. PSF-subtracted, *R*-band coronagraphic image centred on β Pic. North is up and east is left. Bars in the north-east and south-west quadrants represent 10 arcsec and are placed 103.6 arcsec (2000 au) radius from β Pic. The NE disc mid-plane is detected near 2000 au radius, whereas the SW mid-plane is traced to approximately 1000 au radius. Other large-scale extended features in this image are due to instrumental scattered light (e.g. radial linear features, a narrow ring segment in the south-east quadrant, and amorphous structure near a bright star north of β Pic).

investigations of the dynamics of tidally disrupted particle discs, and provide general discussion of the induced asymmetries and particle stripping. In Section 4 we discuss our findings and summarize the conclusions.

2 NEW OBSERVATIONAL RESULTS

New optical coronagraphic observations of the environs of β Pic were obtained with the University of Hawaii 2.2-m telescope on 2000 January 31. A key goal was to maximize sensitivity to the outer regions of the disc. The coronagraph used has 12 interchangeable, circular, focal-plane occulting masks, from which we selected a mask 12.5 arcsec in diameter. This particular mask size is approximately two times larger than the minimum size allowable by the seeing conditions, and it partially obscures the image out to 120 au projected radius about β Pic. However, it also minimizes the scattered light in the field that dominates the background noise. Additionally, the occulting mask increases the efficiency of the observations by maximizing the integration time permitted before saturation of the charge-coupled device (CCD) occurs just beyond its edge.

We obtained 122 integrations of 30 s each through an *R*-band filter ($\lambda \sim 0.67\,\mu$m). Re-imaging optics provided a pixel scale of 0.407 arcsec pixel^{-1} on a 2048×2048 CCD. The field was masked by the coronagraphic focal-plane assembly that has a circular clear aperture with diameter 336 arcsec. The airmass of observation (>3.0), combined with high winds, produced image quality varying from 1.0 to 1.8 arcsec. For final data analysis, we selected 77 frames with the image quality characterized by stellar full width at half-maximum (FWHM) $\leqslant 1.2$ arcsec.

Data were bias-subtracted, flat-fielded and sky-subtracted using the median sky value in the corners of the field for each frame. Comparison stars were also observed for the purpose of subtracting the β Pic PSF. However, this subtraction step adds noise and so we chose to remove the background using an artificial point spread function (PSF). The artificial PSF is a figure of rotation for a seventh-order polynomial that is a least-squares fit to the PSF of β Pic sampled in radial directions perpendicular to the disc mid-plane.

Fig. 1 shows the final image of β Pic with effective integration time 2310 s. The 3σ background noise corresponds to a sensitivity of $R = +25.8$ mag. The mid-plane of the SW extension is difficult to trace visually as a distinct linear feature beyond $\sim$55 arcsec (1062 au), whereas the NE mid-plane is traceable at up to $\sim$95 arcsec (1835 au) radius from β Pic. By these measurements the length asymmetry is approximately 70 per cent.

A key problem in comparing the lengths of the two extensions is that the morphology of the SW extension departs significantly from a linear feature, becoming vertically distended and amorphous at large radii. To compensate for this difference in vertical structure we rotate the image such that the disc mid-plane lies along pixel rows and bin the data in the vertical direction. We do this by summing the light at each pixel location with the light from its two vertically adjacent pixels. This vertical binning procedure smoothes the data and equalizes the NE and SW FWHM measurements when taking vertical cuts at given projected radii along the mid-plane extensions. Smoothed contours of the resulting image are shown in Fig. 2. Here, the 25.0 mag arcsec^{-2} contour traces the NE extension to 95 arcsec radius, and the SW disc extension is traced to $\sim$75 arcsec (1450 au). The length asymmetry by this measurement is therefore $\sim$25 per cent, which is fractionally larger than the length asymmetry measured by Kalas & Jewitt (1995) at about a half of the radial scale probed here. The asymmetric vertical morphology evident in the contours in Fig. 2 also confirms the *butterfly asymmetry* (see Section 3.3) reported by Kalas & Jewitt (1995).

2.1 Summary

The new data reported above show that the β Pic disc has a significantly greater radial extent (1835 au for the NE disc extension; 1450 au for the SW) than has been previously

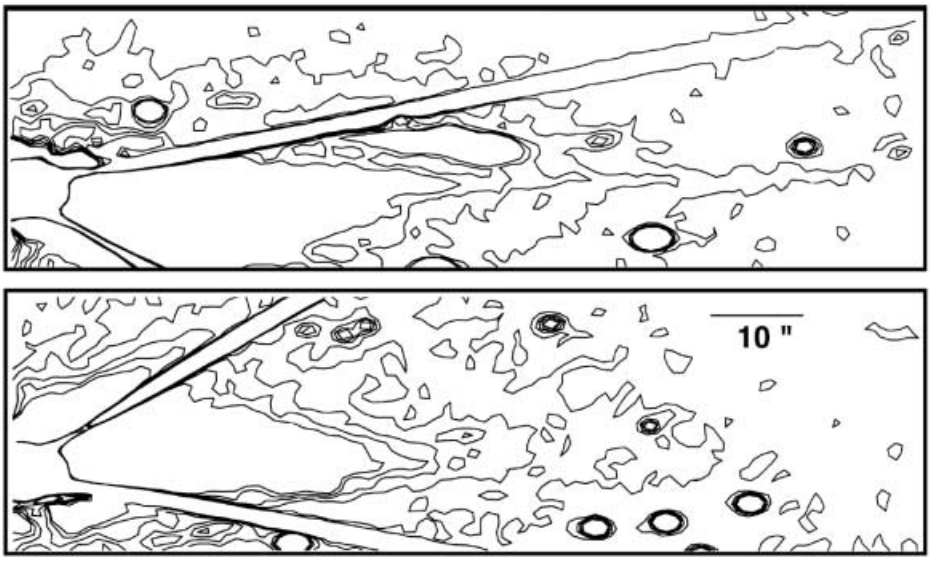

Figure 2. Surface brightness contours for the NE mid-plane (top) and SW mid-plane (bottom). The original image (Fig. 1) has been rotated 60° anticlockwise such that the mid-plane lies along pixel rows. This image is separated along the vertical axis and the NE mid-plane then reflected such that the two sections of mid-plane point in the same direction. The outer contour represents 25.0 mag arcsec^{-2} and has radial extent approximately 25 per cent greater for the NE extension than for the SW extension. The binning procedure for the data is described in the text.

measured. Smith & Terrile (1987) reported the maximum extent of the disc of β Pic at 1300 au (i.e. 67 arcsec) for the NE mid-plane at optical wavelengths. However, this was known as a sensitivity-limited value rather than the true physical extent of the disc. Here too we are unable to define the outer disc extents above the level of the background noise.

The existence of a disc mid-plane out to $\sim 10^3$ au radius, as well as the $\sim 10^2$ au vertical thickness of the SW extension (see fig. 4 in Kalas & Jewitt 1995), is unexpected given our current understanding of planetesimal formation as applied to the Solar system (reviewed by Weidenschilling & Cuzzi 1993). Thus we must conclude that planetesimals were created at much smaller radii than they are presently inferred to exist in β Pic, and subsequently suffered redistribution. Moreover, this redistribution must allow for the existence of a lopsided and vertically flared disc. Global redistribution of this kind is a general outcome of a close stellar fly-by encounter (KLSS). Below we shall present numerical investigations of the dynamics involved.

3 DYNAMICAL MODELS

In the fly-by model presented in KLSS a transient system of circumstellar eccentric rings was found to form in the perturbed disc of particles, as shown in Fig. 3. Fly-by parameters, and viewing angle and epoch, were chosen to give the most satisfactory fit possible to the positions of the mid-plane brightness peaks found in the observations, and to the large-scale disc asymmetries. The model presented in KLSS will serve here as a reference case with which we compare the model behaviour as we vary the parameters about its particular values. In that model the computational length unit scaled to $\sim$270 au, with the initial disc radius (2 units) and distance of pericentre (2.6 units) for the perturber being $\sim$540 au and $\sim$700 au respectively. Since G and the primary mass were set to unity in the computations, the computational time unit scaled to $\sim$530 yr (i.e. the period at unit radius divided by 2π). Their system of computational units is used here in similar numerical simulations; however, we point out that the scalings mentioned above are only used for reference, in order to maintain generality in the presentation of our results.

The new numerical calculations presented below employ a fifth-order accurate Runge–Kutta–Fehlberg integrator with a variable time-step size. While not as accurate as the Bulirsch–Stoer method (e.g. as used by Hall et al. 1996), this method allows for the fast integration of much larger numbers of particles ($\sim 10^{4-5}$) with moderate accuracy. Time-step size control is implemented as described in Press et al. (1992), by specifying a maximum relative error ϵ in the velocity magnitude. The value of ϵ was taken to be as small as practicable. Unless stated otherwise we take $\epsilon \sim 10^{-9}$. Thus, in a typical run of $\sim 10^5$ time-steps, the net relative error in the energy and angular momentum of any given particle is $\sim 10^{-4}$. In practice the net relative error for most of the particles will be substantially smaller than this since the time-step size is controlled by a minority of particles that fall close to either of the stellar masses. To prevent too large a reduction in the time-step size as a result of this effect, we remove particles from the calculation if they approach either star to within a radius R_p of the primary or a radius R_s of the secondary. Unless stated otherwise we take: $R_p = 0.03$ and $R_s = 0.01$. The former value was chosen as the minimum required to ensure that the time-step size would not be controlled by close approaches of particles to the primary rather than by close approaches to the secondary, for all model parameters considered here. The secondary was integrated as if it were a test particle in motion about a fixed primary of mass equal to the total binary mass. The gravitational forces on particles are then prescribed as a function of position at each time level with the addition of a fictitious force to compensate for the non-inertial origin (see below). As mentioned above, the test particles are collisionless and their distribution is taken as a tracer of the observed dust presumed to be produced by infrequent collisions in the real system.

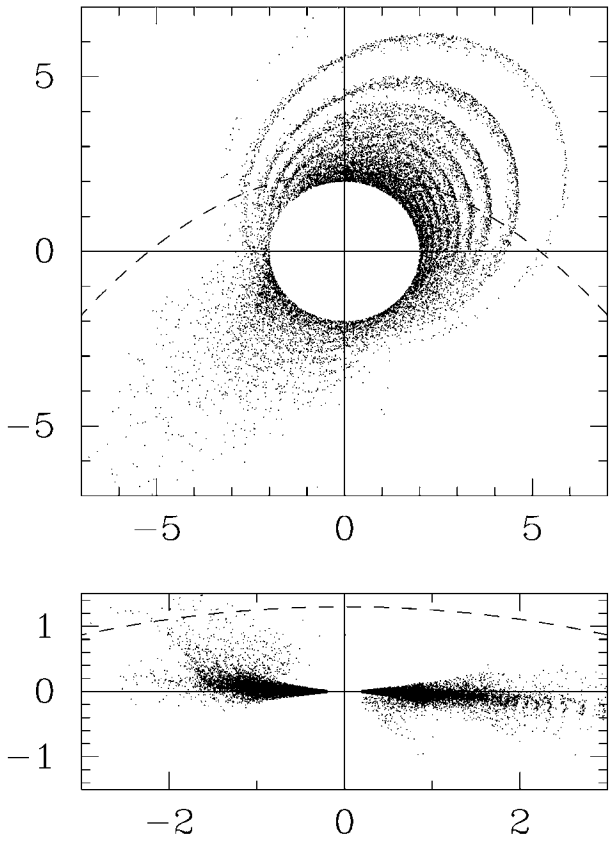

Figure 3. The face-on and edge-on views of a sample of simulation particles in the computational frame centred on the primary mass (labelled fig. 2 in KLSS). The primary is of unit mass and $G = 1$, giving a time unit such that the circular orbit period at unit radius is 2π. The horizontal axes correspond to the line of nodes of the perturber's orbit. Parameters are: perturber mass of 0.3, parabolic pericentre distance of 2.6, pericentre inclination of 30°. The disc of $\sim 10^6$ particles is initially distributed between 0.2 and 2 radius units. The initial vertical density is exponentially decreasing, with an outer height of 0.6, and the aspect ratio and the radial surface density follow radial power laws of index -1.5. A random sample of $\sim$25 per cent of the particles outside the initial radius are shown in the top frame, the bottom frame shows a thin slice of particles about the horizontal axis. The path of the perturber is indicated with a dashed line and it enters the frame from the right-hand side. The positions and velocities of the particles are integrated with a second-order leapfrog scheme; the perturber orbit is prescribed as a function of time. The configuration shown is for a time of 160 units after pericentre passage. The perturber was introduced at a separation from the primary of 20 units.

The origin of time is taken as the instant of pericentre passage, hence computational time levels may be negative or positive. Throughout we shall use 10^4 test particles initialized in Keplerian circular coplanar (zero-inclination) orbits, placed at random in the radial interval 0.5–2 such that the surface density profile decreases according to a power law of radius$^{3/2}$. The perturber has initial

position and velocity components appropriate to the chosen orbital inclination, eccentricity and mass. The perturber is initialized at a distance of 10 times the initial outer disc radius (i.e. at 20 units). We shall consider a single pericentre distance of $q = 2.6$ units, and thus the initial disc size is $\sim 0.8q$. The length and mass units, and therefore the time unit, used in our calculations can be scaled so as to apply to any system within the range of dimensionless parameters that we cover. Thus, given our choice of relative disc size, fixing q does not affect the generality of our models. Also, since the initial disc is axisymmetric, the longitude of periastron for the perturber orbit is arbitrary. In all our particle position plots the perturber orbit is oriented as in Fig. 3, except for differences in orbital inclination.

3.1 Circumstellar ring formation

In order to identify the dynamical origin of the ring features simulated by KLSS, we consider the system response to different components of the tidal potential [an approach also used recently by Pfalzner & Kley (2001) for gas discs]. The total potential is given by $\Psi = \Psi_p + \Psi_s$, where the point-mass potential at position $\boldsymbol{r}$ due to a primary of mass M_p, to which we have fixed the origin, is

$$\Psi_p = -\frac{GM_p}{|\boldsymbol{r}|}. \tag{1}$$

The tidal potential due to the secondary with mass M_s and instantaneous position $\boldsymbol{r}_s$ is given by

$$\Psi_s = -\frac{GM_s}{|\boldsymbol{r} - \boldsymbol{r}_s|} + \frac{GM_s \boldsymbol{r}\cdot\boldsymbol{r}_s}{|\boldsymbol{r}_s|^3}. \tag{2}$$

The first term on the right-hand side of equation (2) is the direct potential due to the secondary star; the second term is the indirect potential due to the acceleration of the origin. In a stellar fly-by this acceleration corresponds to the reflex motion of the primary star due to a gravitational tug from the secondary star.

In Fig. 4 we give particle position plots for fly-by simulations in which we: use only the direct term in the tidal potential, use only the indirect term in the tidal potential, and use the full tidal potential. In the case that employs only the direct tidal term, the disc is pulled towards the perturber as it approaches pericentre. In the case using only the indirect tidal term, the disc is repelled by comparison as the perturber approaches pericentre (in the inertial frame this effect corresponds to acceleration of the primary towards the secondary). In these first two cases eccentric nested rings are observed to form, although they appear as stronger features in the case where only the indirect tidal term is used. Since the effectiveness of the direct tidal interaction depends on the disc being able to approach the perturber closely, the role of the indirect tidal term when the full tidal potential is used is towards weakening the ring features that result from the direct tidal interaction, and to cause approximate pericentric anti-alignment of the two sets of rings. This scheme in the alignment of the particle orbits gives a length asymmetry between opposing sides of the disc when viewed edge-on, with the strongest ring features along the longest extension.

In the above the features that appear to be ring-like are actually formed from distended tightly wound one-armed kinematic spiral patterns. Different levels of advancement in the winding process can be seen at the third and fourth time levels depicted in Fig. 4. This is more clearly illustrated in Fig. 5 where we plot particle positions according to the *true anomaly* (i.e. the angle between the instantaneous position vector and the line of pericentre) for the last frame given in Fig. 4 and for a time much later after pericentre passage, for the model using only the indirect term in the tidal potential. [Although we have now identified the origin of the ring features, since over much of the azimuth the appearance of the features resembles nested eccentric rings, we shall continue with our original usage of that description.]

Winding of the kinematic spiral occurs as particles move around their orbits with local orbital frequency Ω. Thus the time-scale for the generation of a ring after pericentre passage is Ω^{-1}. The lack of significant width to the spiral in Fig. 5 as compared to Fig. 4, indicates that the width of the rings is mainly due to the spread in the particle eccentricities. The rings will appear to propagate outwards and dissolve as a result of the growth of incoherence in the phase relationships of particles. Consider two neighbouring particles at radii or semimajor axes a_o and a_i, where $a_o > a_i$. The decoherence time-scale t_d for the particle pair is given by

$$t_d^{-1} = \frac{\Omega(a_i)}{2\pi}\left[1 - \left(\frac{a_i}{a_o}\right)^{3/2}\right]. \tag{3}$$

In β Pic, and the simulations, the width of the mid-plane brightness features is ~5–10 per cent of their radii (KLSS). For dissolution of the ring features we require the tight winding of a spiral down to the scale of a ring width; thus for a ring at radius r

$$t_d \sim 10^5 \left(\frac{r}{500\,\mathrm{au}}\right)^{3/2} \mathrm{yr}. \tag{4}$$

This agrees with the simulations of KLSS in which it is found that the ring features dissolve in about 10 local orbital periods. KLSS also found that viewing the perturbed model disc at approximately 10^5 yr after pericentre passage gave the most satisfactory fit to the observed disc, which is consistent with the innermost ring feature being detected at ~500 au.

3.2 Length asymmetry in coplanar models

As discussed above, a length asymmetry in the disc is readily obtained from a close fly-by encounter. The length asymmetry in the disc of β Pic is also the most easily measured of its asymmetric features. Below we shall continue to investigate numerically the form and size of the length asymmetry as a function of fly-by parameters.

3.2.1 Parabolic versus hyperbolic trajectories

A secondary star of orbital eccentricity e with respect to the primary star has relative velocity magnitude V_q at pericentre distance q given by

$$V_q^2 = (1 + e)\frac{G(M_p + M_s)}{q}. \tag{5}$$

Hence for the scaling used by KLSS, eccentricities of 1, 2, 5 and 10 correspond to pericentre velocities of ~2.5, 3.1, 4.3 and 5.9 km s^{-1} respectively. In this section we shall consider coplanar encounters of uniform pericentre distance 2.6, a perturber mass of 0.3 and these orbital eccentricities. The corresponding trajectories and the initial disc size used in these simulations are shown in Fig. 6.

A useful diagnostic measure of the length asymmetry induced

in the disc is given by plotting the final apocentre distance against the longitude of pericentre for each perturbed particle orbit. By *final* we shall mean that the secondary mass has passed through pericentre and has returned to a sufficiently large radius that its effect on the positions and velocities of the particles bound to the primary is negligible. In our simulations we integrated the system for a total time of 120 units, which means that the final perturber distance was always much greater than the initial distance, corresponding to a time of at least 80 units after pericentre passage. This total run-time was also generally required in order for the numbers of particles either bound or unbound to each of the two stellar masses to stabilize (in practice this meant to approach a constant value with less than about 10 per cent fluctuations; cf. Hall et al. 1996). This information is summarized in Table 1, for all the $e \geqslant 1$ models presented in this paper.

In Fig. 7 we compare the disc response for encounters of different eccentricity. In all cases there are two oppositely directed extensions. The extension near to a longitude of -2 contains the strong ring features, and the other extension (near longitude $+1$) contains the weak ring features, as discussed above. Respectively we shall refer to these as extension A and extension B. Thus extension A forms as a response to the indirect component of the

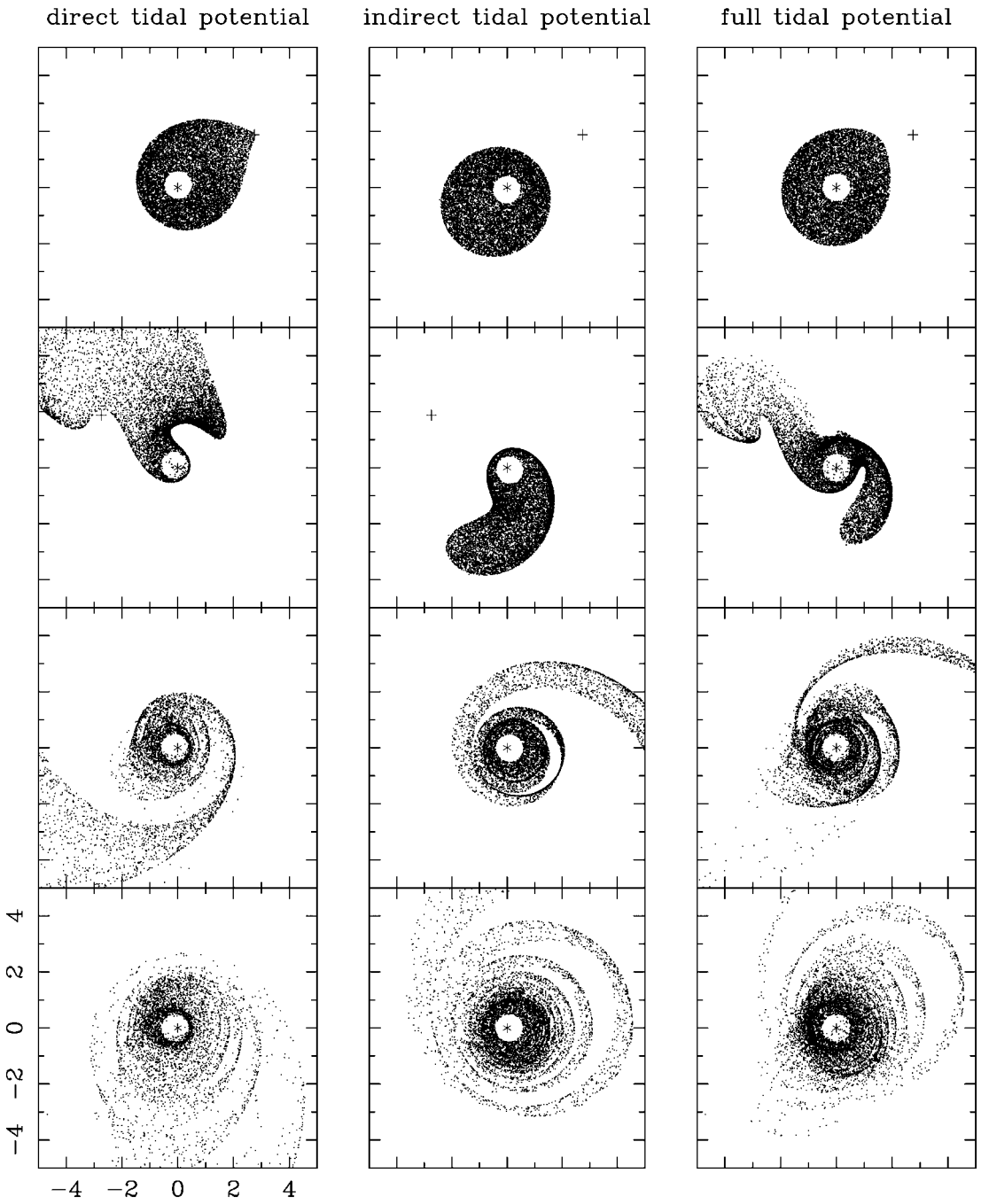

Figure 4. Particle positions at various times for parabolic fly-by encounter simulations that use different components of the tidal potential. From the top row of frames to the bottom the times given are -3, $+3$, $+20$ and $+60$. The perturber is plotted with a cross, and the primary star (origin) is plotted with an asterisk. In these simulations we used $\epsilon = 10^{-7}$, $R_p = 0.1$ and $R_s = 0.05$ and removed particles that went beyond radii greater than 10 from the primary.

tidal potential, and extension B forms as a response to the direct component of the tidal potential.

As the encounter velocity (equivalently, the orbital eccentricity) increases, the peak of extension A diminishes in amplitude, while the peak of extension B increases its amplitude. Further examination of the extension B results illuminates a key difference between the parabolic ($e = 1$) and hyperbolic ($e > 1$) orbit cases. In the former, extension B is compact, but in the latter cases all show a much longer extension B. In Fig. 8 we show the final apocentre distance against the longitude of pericentre for the parabolic case in which only the direct part of the tidal potential is used. As we might have expected, extension A is not in evidence (being due to the indirect part of the tidal potential), and extension B is similar in nature to that found in the hyperbolic orbit cases. Thus we conclude that in the full tidal potential case the indirect component acts on the disc prior to pericentre passage such that the disc response due to the direct component near pericentre is modified as compared with a calculation that uses only the direct term (also discussed in Section 3.1). Hence the more impulsive (i.e. hyperbolic) encounters yield a response that is similar to that found for the parabolic case that uses the direct term only, being manifest in the form of extension B. It follows that higher velocity (i.e. more eccentric) perturbers will have extension B forms more like that found in Fig. 8, and smaller amplitudes for extension A. This can be seen in Fig. 7.

In Fig. 9 we give the final eccentricities of the disc particles for different eccentricities. In the parabolic orbit case, extension A particles correspond to the wing-shaped distribution having eccentricities approximately in the range 0.2–0.6. Superposed with this are the extension B particles that have generally very high eccentricities. The change in the relative lengths of extensions A and B with increasing perturber eccentricity is also apparent. Generally, the excited eccentricities of the disc particles are lower for larger perturber eccentricities, which can be explained from the simplistic impulse model for tidal interaction (Lin & Papaloizou 1979): higher relative velocity results in weaker coupling between the particles and the perturber.

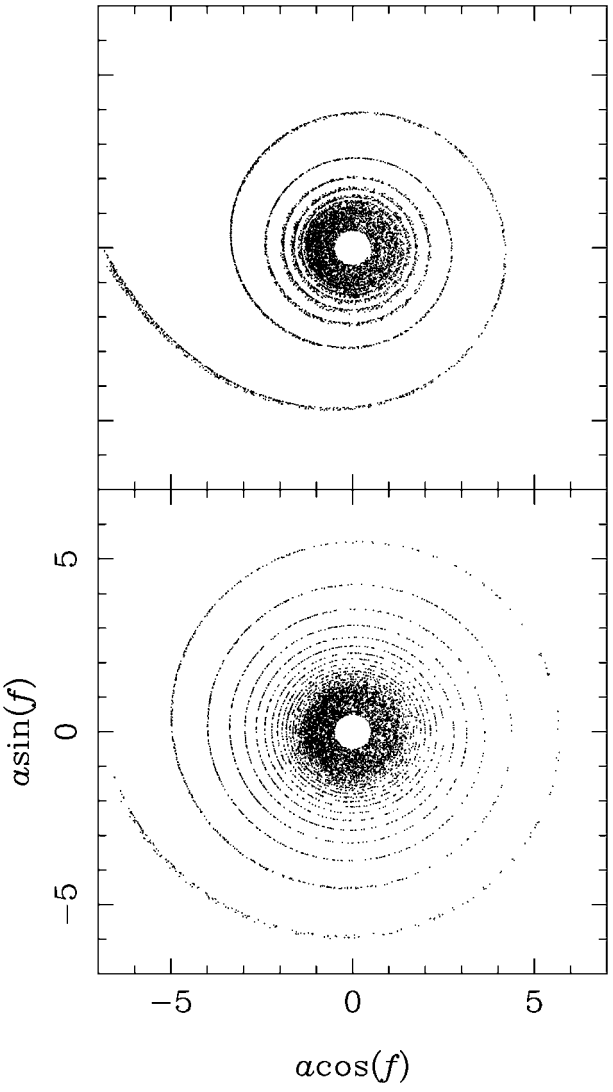

Figure 5. Data for the model using only the indirect component of the tidal potential (see Fig. 4). The top frame is for data taken at a time of +60; the bottom frame corresponds to a time of +180. Plotted are $a\cos f$ against $a\sin f$ for each particle, where a is the semimajor axis and f is the true anomaly.

3.2.2 *Variation of the perturber mass*

In Fig. 10 we show the final distance of apocentre against the final longitude of pericentre for parabolic encounters with different

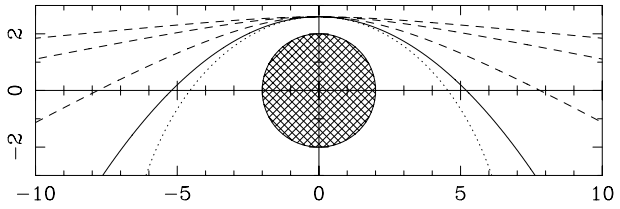

Figure 6. Schematic representation of the initial disc (cross-hatched circle), and the orbital paths of a perturber for a parabolic encounter (solid line) and hyperbolic encounters (dashed lines, from lowermost to uppermost, for $e = 2$, 5 and 10 respectively). The dotted line corresponds to a bound orbit with $e = 0.75$ (see Section 3.5). As for the simulations, the origin is assumed to be fixed to the primary.

Table 1. Data for some fly-by encounter models. The mass of the secondary relative to the primary is μ, the orbital eccentricity of the secondary is e, and the orbital inclination of the secondary is i. The length ratio of extension A to extension B is L. We also give the percentage of the initial particle number that is ultimately: bound to the secondary star (n_b), deleted by entering the secondary star's accretion radius (n_s), deleted by entering the primary star's accretion radius (n_p), or unbound from the system (n_u). The model listed in the third row was deemed to be most appropriate for modelling the asymmetries in the β Pic disc (KLSS; also Fig. 3).

μ	e	i (deg)	n_b	n_s	n_p	n_u	L
0.1	1	0	6	2	0	3	$\ll 1$
0.3	1	0	12	5	0	4	1.5
0.3	1	30	11	0	0	5	1.2
0.3	1	60	0	0	0	0	$\ll 1$
0.3	2	0	9	0	1	12	0.3
0.3	2	30	8	0	0	8	$\ll 1$
0.3	5	0	0	0	0	7	$\ll 1$
0.3	10	0	0	0	0	1	$\ll 1$
0.5	1	0	16	1	6	5	$\gg 1$
1.0	1	0	21	2	8	17	$\gg 1$

masses for the perturber. We consider the mass ratio $\mu = M_s/M_p$. Increasing the perturber mass from $\mu = 0.1$ to $\mu = 1.0$, we find that extension A increases in amplitude and extension B diminishes in amplitude. The former effect is due to the larger perturber mass inducing a larger-amplitude reflex motion of the primary star; the latter effect evidently results from the more massive perturber being able to strip more particles from the disc in the direct interaction that sets up extension B (see Section 3.4).

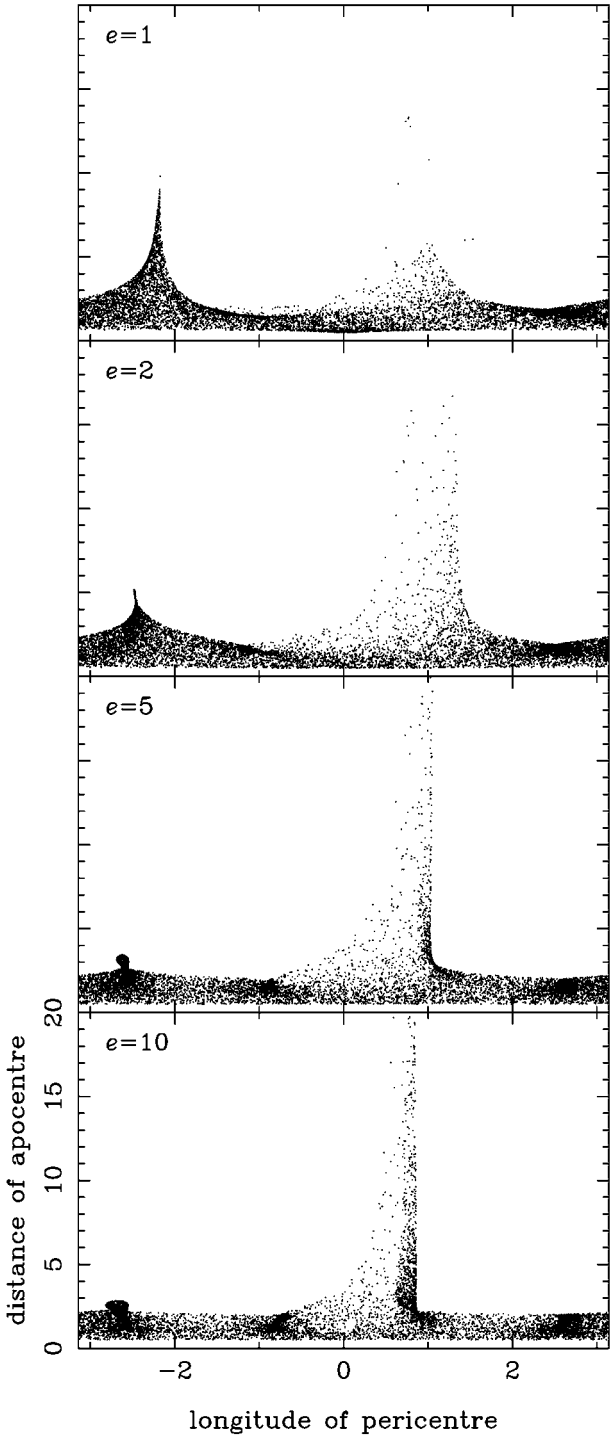

Figure 7. The final distance of apocentre against the longitude of pericentre for fly-by simulations with perturber orbits of eccentricity $e =$ 1, 2, 5 and 10. Here and in similar plots we select particles with $e < 1$ and with separations from the secondary of greater than 10, at the final time level. In all plots involving the longitude of pericentre, zero longitude is defined by the positive horizontal axis in face-on particle position plots.

The lowest-mass model with $\mu = 0.1$ has an extension B that has a similar extended form to the high-eccentricity cases discussed above. This is due to the low mass of the perturber giving only a small reflex motion of the primary, and so a relatively weak interaction prior to pericentre passage, which necessarily results in a more impulsive response. Only the $\mu = 0.3$ model gives a compact extension B and extension A. This case has, in terms of a model for the length asymmetry in the disc of β Pic, the most appropriate amplitude ratio for the extensions A and B of those coplanar models tried here. The ratio of lengths of apocentre for this model is approximately $9/6 = 1.5$, the length ratios of the other models clearly being very different from unity. The length ratio between extensions A and B is given in Table 1, for all our models with $e \geqslant 1$. Where the ratio is clearly much different from unity we simply state either $\gg 1$ or $\ll 1$, since the interpretation of the length of an extension as defined by a small number of particles at large distances is not clear.

We note that the size of extension A can be reduced by increasing the eccentricity of the perturber, so it may be possible that a more massive ($\mu > 0.3$) and eccentric orbit ($e \gtrsim 1$) perturber could fit the observational results. However, since eccentricities larger than approximately unity do not display a compact extension B, we favour the perturber mass originally considered by KLSS (i.e. $\mu \sim 0.3$, for $e \sim 1$).

3.3 Inclined orbits

In general, if the perturber's orbit and the initial disc plane are not coplanar, then the tidal interaction occurring between the disc particles and the perturber can excite vertical motions in the particle orbits. Here we shall consider this effect in terms of the inclination i of the perturber's orbit to the initial disc plane. This angle is generated by rotating the perturber's orbit about the *latus rectum* (i.e. the line perpendicular to the line of pericentre, which also passes through the origin), which then becomes the *line of nodes* (e.g. see Fig. 3).

KLSS found that (for $i = 30°$) extension B became vertically flared, with much weaker inclinations in extension A, as can be

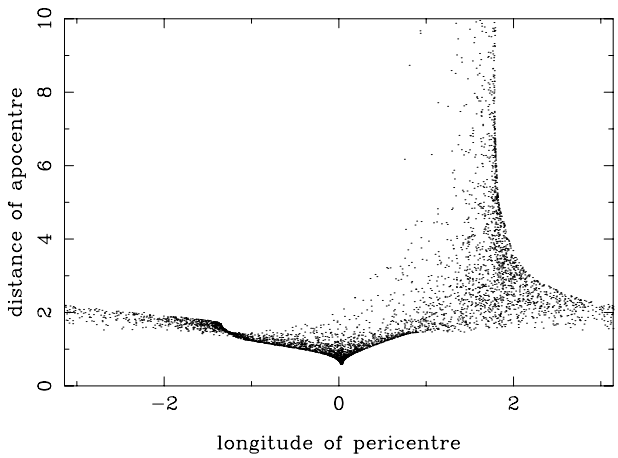

Figure 8. The final distance of apocentre against the longitude of pericentre for a fly-by simulation with a parabolic perturber orbit in which only the direct tidal potential has been used. Data correspond to those given in Fig. 4.

seen in Fig. 3. From the preceding discussion we deduce that the flaring results from the stronger direct tidal interaction, and the smaller inclinations generated in extension A result from the weaker indirect tidal interaction. The resulting morphology resembles the butterfly asymmetry (Kalas & Jewitt 1995; KLSS) in which the vertical height of the imaged disc is greatest north of the mid-plane in the south-west extension (see Figs 1 and 2), and south of the mid-plane in the north-east extension, with the overall greatest vertical height in the former.

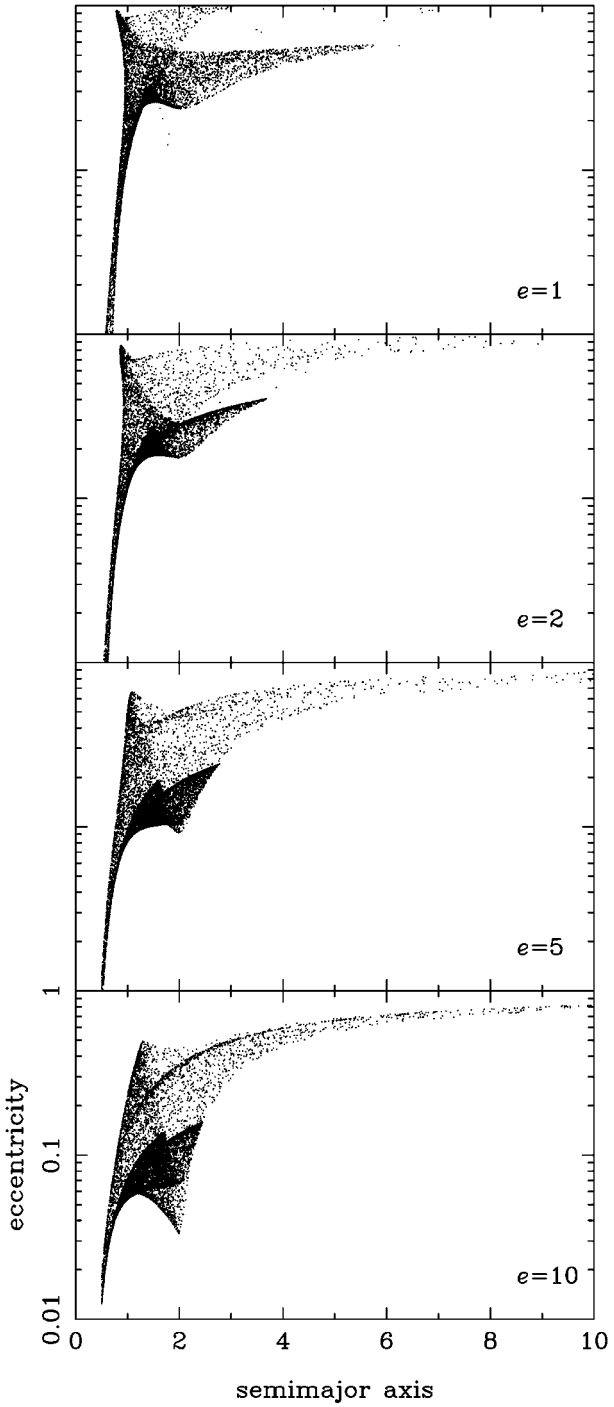

Figure 9. The final eccentricity against semimajor axis distribution for fly-by simulations with perturber orbits of eccentricity $e = 1$, 2, 5 and 10.

3.3.1 Length asymmetry

In Fig. 11 we give the final distance of apocentre against the longitude of pericentre for parabolic encounters with $\mu = 0.3$, and $i = 30°$ and $i = 60°$. In the lower-inclination case the disc response is very similar to the coplanar encounter presented above, except that extension A is shorter by about 20 per cent. In the higher-inclination case the response resembles that of a

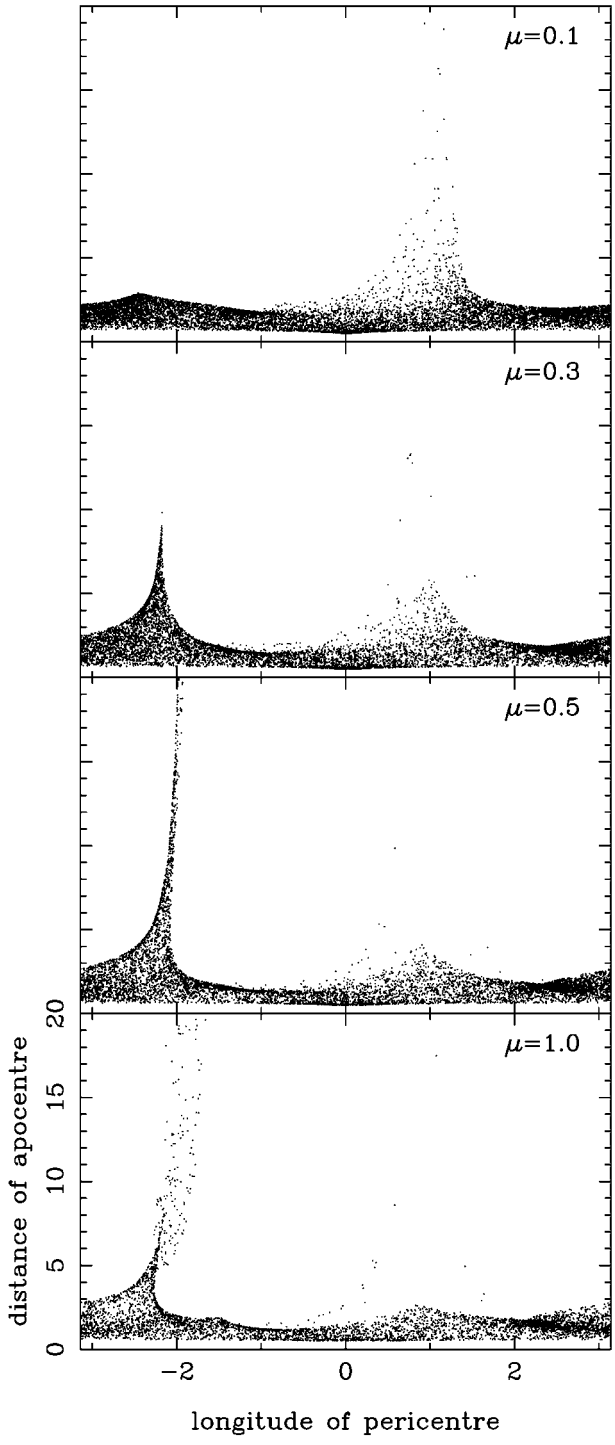

Figure 10. The final apocentre distance against longitude of pericentre distribution for parabolic fly-by simulations with perturber masses of 0.1, 0.3, 0.5 and 1.0.

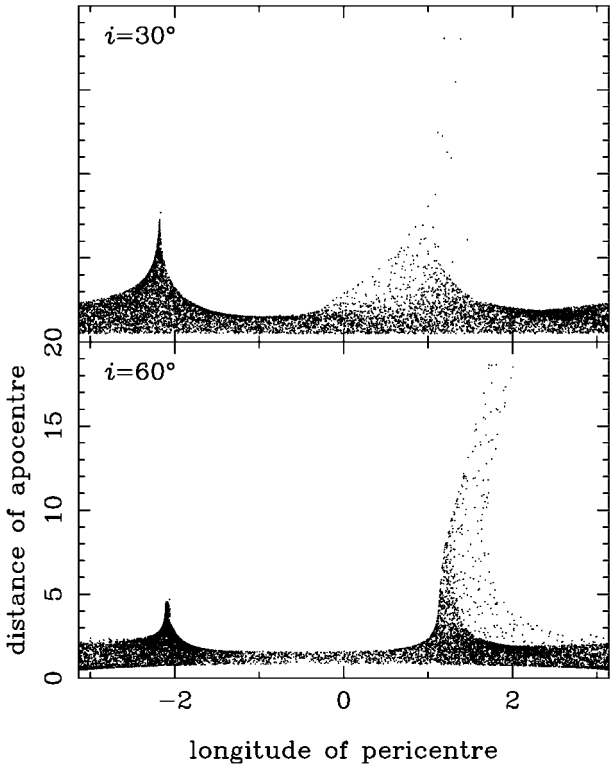

Figure 11. The final distance of apocentre against the longitude of pericentre for parabolic fly-by simulations with orbital inclination $i = 30°$ and 60°.

coplanar hyperbolic encounter, having a very short extension A and a very long extension B. As before, this is consistent with the notion that the disc interaction prior to pericentre passage is a key difference between hyperbolic and parabolic encounters. In the $i = 60°$ case the high inclination takes the perturber orbit further from the disc, making the pericentre interaction more impulsive. This shows that we require an orbit with not too high an inclination, if we wish to preserve the compact nature of extension B. Additionally, the other angle possible, which corresponds to rotation of the orbit about the line of pericentre, need not be considered since for low values of i that angle takes the orbit yet further from the disc. In other words, we only consider an argument of pericentre of 90°.

In the higher-inclination case the length ratio of extension A to extension B is clearly much less than unity. In the lower-inclination case extension B is compact, but the peak is less distinct than for the coplanar case. We measure its height by taking the intersection of the tangents to the sides of the envelope of the extension particles near its base. This yields a height of approximately 6, which is similar to the coplanar model. Thus we deduce a ratio $7/6 \sim 1.2$. This is the best-fitting value, in terms of the length asymmetry, of those models presented in this paper. Scaling according to the KLSS model, the lengths of the extensions are 1890 au and 1620 au, which is in good agreement with the new determination of the size of the disc presented in Section 2.

The exact numerical value of the length ratio determined for the β Pic disc could be recovered in our models by taking a slightly smaller orbital inclination than 30°. That would not be productive at this stage, however, since here we are not concerned with the details of translating our results into a scattered-light disc model,

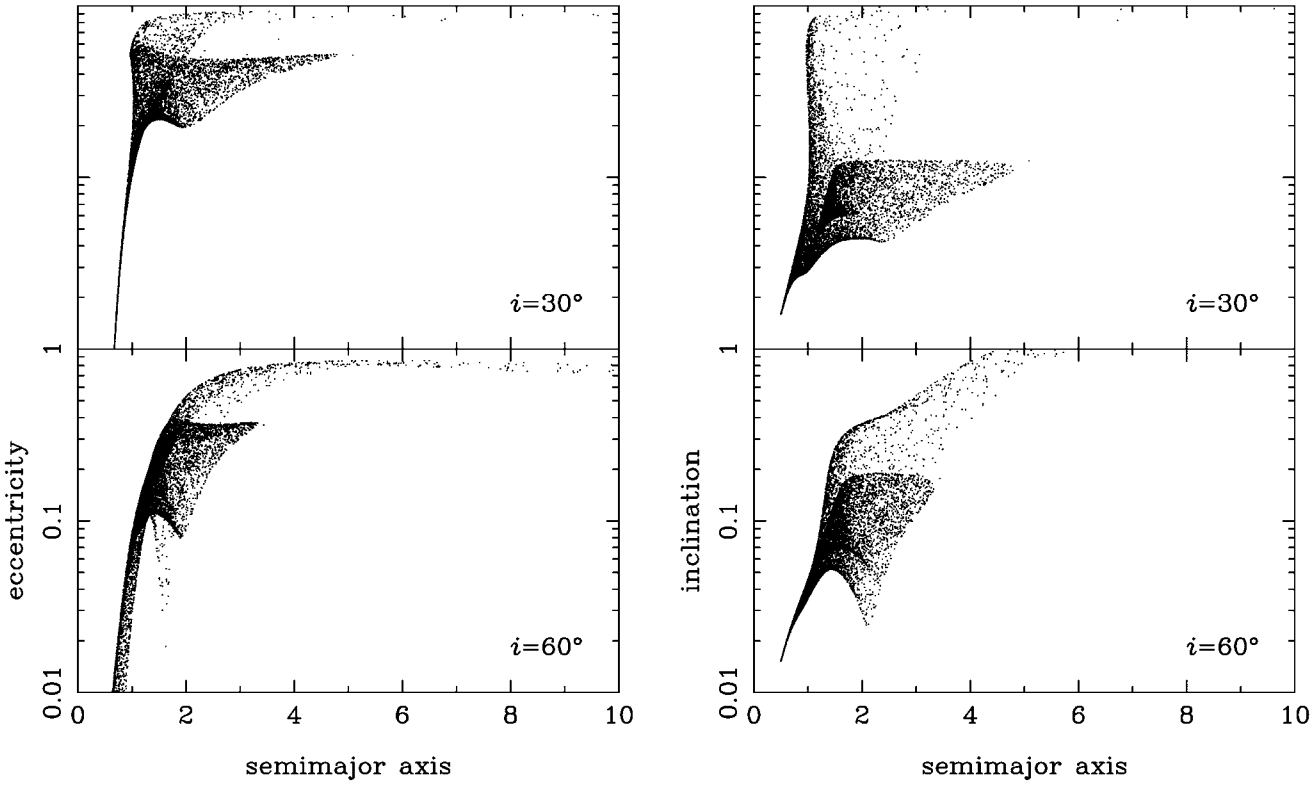

Figure 12. The final eccentricity and inclination against semimajor axis distributions for parabolic fly-by simulations with orbital inclination $i = 30°$ and 60°.

which could introduce a small correction factor. However, for reference, a model with $i = 15°$ was tried and was found to give a length ratio of 1.4. Thus we expect the appropriate inclination to lie between 15° and 30°, i.e. closer to the lower-inclination model above than to coplanar.

3.3.2 *Flaring and warps*

In Fig. 12 we show the final eccentricity and inclination distributions for the disc particles in the two cases mentioned above. The amplitude of the response is lower for higher values of i, for the reasons indicated above. The eccentricity response resembles that of a coplanar hyperbolic orbit, as expected from the preceding discussion. The inclinations associated with extension A are much smaller than for those associated with extension B. However, the extension A inclinations are higher in the $i = 60°$ model, owing to input from the direct interaction because of increased impulsiveness of the interaction occurring at the ascending node in that case. Thus, by symmetry of the orbit with respect to the initial disc, we expect the inclinations in each extension to become comparable when orthogonality is approached by increasing i. This provides a further need for a low-inclination encounter as the disc of β Pic is strongly lopsided with respect to vertical flaring (Kalas & Jewitt 1995).

For these two cases we also give the final pericentre distance distributions in Fig. 13. In the low-inclination case we see that particles from extension B can plunge to pericentre distances of 0.2. KLSS proposed that these particles could explain the existence of an inner 'warp' in the scattered-light dust disc of β Pic at ~50 au (Burrows et al. 1995; Mouillet et al. 1997). We can see from Fig. 13 that, for the higher-inclination encounter, extension B particles have significantly higher perturbed pericentre distances (down to about 0.7, or ~200 au). This is a direct consequence of the lower eccentricities produced at comparable semimajor axes in extension B for the two cases. Thus the minimum pericentre distance is minimized in coplanar cases. Correspondingly, larger minimum pericentre distances are also characteristic of hyperbolic encounters. Fig. 14 gives the final eccentricity and pericentre distributions for a hyperbolic encounter with $e = 2$ and $i = 30°$. If the explanation of the inner warp suggested by KLSS is confirmed, then this also supports the need for a low-inclination and low relative velocity encounter.

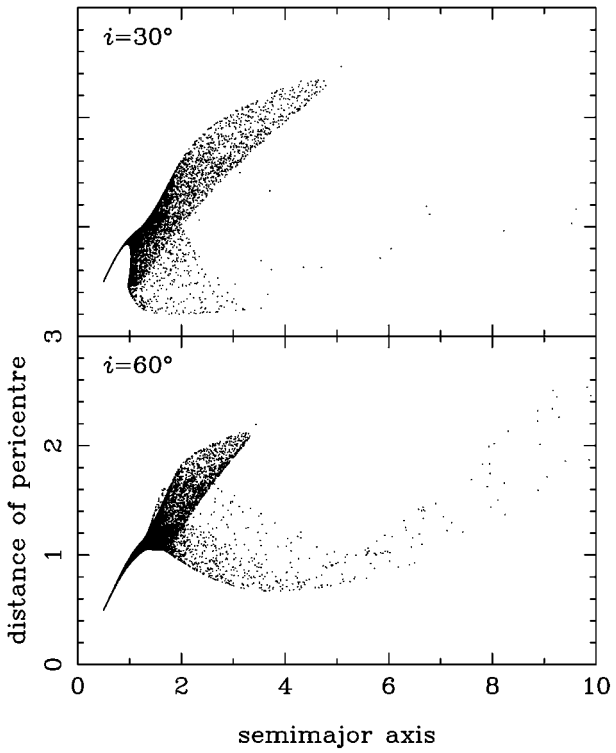

Figure 13. The final distance of pericentre against semimajor axis for parabolic fly-by simulations with orbital inclination $i = 30°$ and 60°.

3.4 Planetesimal capture

As can be seen in Fig. 4 the close fly-by of a disc of particles by a perturbing star can result in the very close approach of some of the disc particles to the perturber. Since the unperturbed disc does not extend all the way out to pericentre, this occurs by particles streaming through the vicinity of the instantaneous Lagrange point between the two stars, about the time of closest approach. In the case that particles become captured by the perturber the capture efficiency is generally low (see also Hall et al. 1996). Table 1 gives the percentage of initial disc particles that are captured by the perturber for the models discussed above, and from it we can

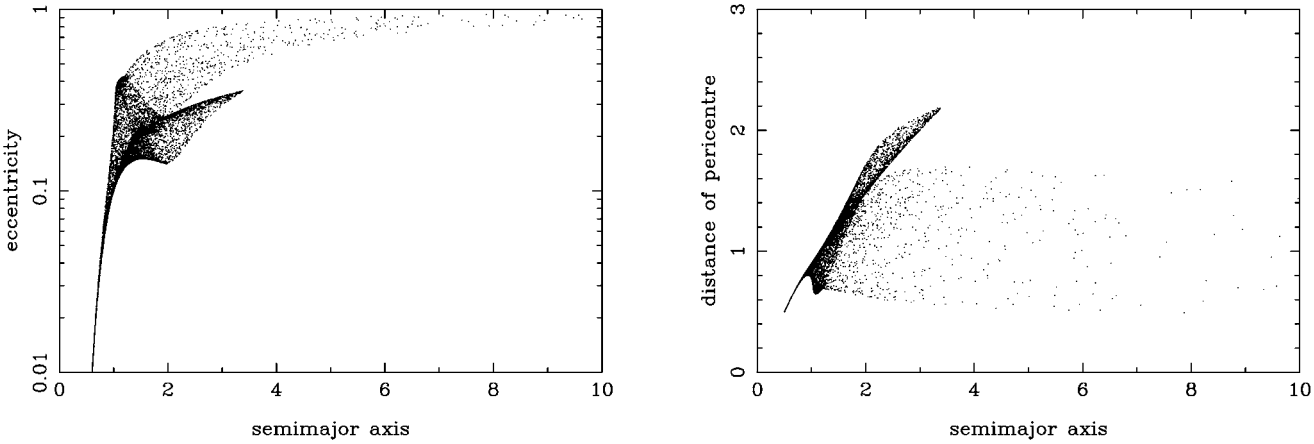

Figure 14. The final eccentricity and distance of pericentre against semimajor axis for a hyperbolic fly-by simulation with orbital eccentricity $e = 2$ and orbital inclination $i = 30°$.

see that the lower-eccentricity and lower-inclination encounters are required, in order to effect capture at all.

For the model parameters used by KLSS, the percentage of captured particles is ~10 per cent of the initial particle number, but note that if the initial disc were allowed to extend to pericentre this figure could be fractionally larger (Hall et al. 1996). In the case of β Pic, considering the maximal parent body disc of Backman & Paresce (1993), the captured material could therefore represent up to about 10^3 Earth masses of planetesimals which would subsequently orbit the perturber and produce a scattered-light signature similar to Vega-like sources. This would not however uniquely identify a perturber candidate since approximately 15 per cent of main-sequence stars of all types are known to have such discs (Backman & Gillett 1987; Aumann 1988), but given the encounter parameters we find here, it seems likely that a perturber candidate should have this signature.

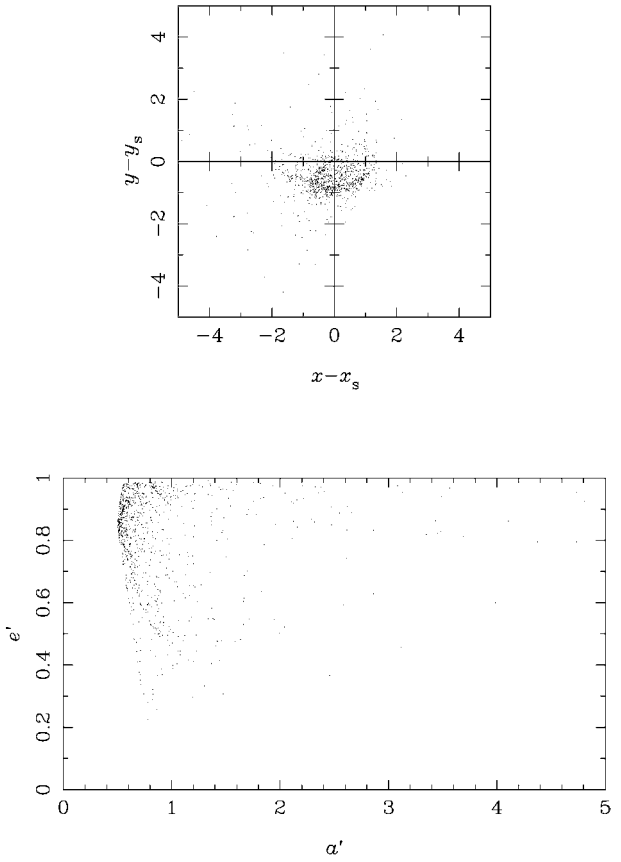

Figure 15. Particle positions and eccentricity versus semimajor axis for captured particles relative to the perturber.

None the less we may find crude approximations for the orbital properties of the captured planetesimals. We shall make an analogy with the theory of mass transfer in semi-detached binaries, in which the captured matter orbits the secondary with the specific angular momentum of relative motion at the Lagrange point (see Frank, King & Raine 1992). Here we deduce that, if a particle in the outermost parts of the disc is captured close to the perturber's pericentre, then it will orbit the perturber with specific angular momentum

$$\left[\sqrt{\frac{G(1+e)(M_\mathrm{p}+M_\mathrm{s})}{q}}-\sqrt{\frac{GM_\mathrm{p}}{R_\mathrm{o}}}\right]b, \tag{6}$$

where R_o is the initial outer radius of the disc and b is the separation of the secondary from the Lagrange point at the instant of pericentre passage, approximated by

$$b/q=\tfrac{1}{2}+0.227\log\mu. \tag{7}$$

In the above we have taken the circular velocity of a particle lying on the binary axis relative to the perturber at pericentre for the input particle velocity. Although the instantaneous Lagrange point is located well within the envelope of the initial disc, the rapid eccentricity changes in the disc prior to particle transfer cause compression of the disc such that the outer disc particles pass through the vicinity of the Lagrange point with approximately their initial velocities (e.g. see Fig. 4).

With respect to the perturber, the specific angular momentum of the captured particle is $\sqrt{GM_s a'(1-e'^2)}$, where the characteristic semimajor axis and eccentricity with respect to the secondary are respectively a' and e'. Hence we have:

$$a'(1-e'^2)=q(1+e)\frac{(1+\mu)}{\mu}\left(\frac{b}{q}\right)^2\left[1-\sqrt{\frac{q/R_\mathrm{o}}{(1+e)(1+\mu)}}\right]^2. \tag{8}$$

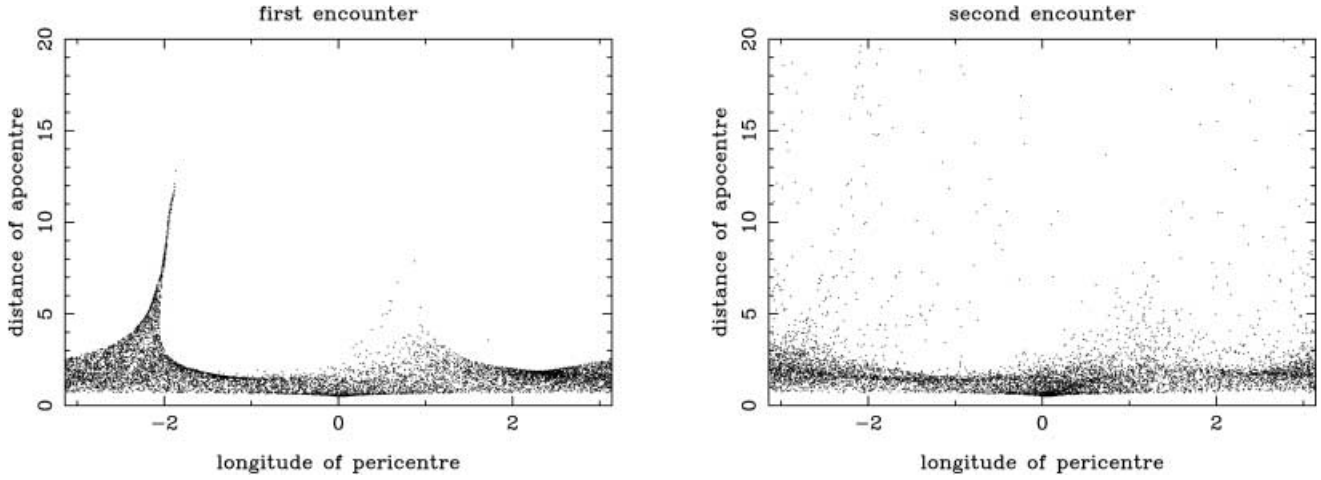

Figure 16. The final distance of apocentre against the longitude of pericentre for a bound orbit fly-by simulation with $e=0.8$. The companion starts at apocentre and was set up and integrated much as for the hyperbolic orbit cases. Data are given for the first and second complete orbits. In this simulation we used $\epsilon=10^{-7}$.

Thus for a model with $e = 1$, $\mu = 0.3$ and $q = 2.6$, we find $a'(1 - e'^2) \sim 0.3$. This equation does not apply when the relative velocity of the perturber and disc particles is sufficiently high that particle transfer is energetically disallowed. As shown in Table 1 we find that particles are captured when $e \leqslant 2$ but not when $e \geqslant 5$.

The above is in fair agreement with the simulations. In Fig. 15 we give the positions, eccentricities and semimajor axes of captured particles relative to the perturber for the above model. We find that the bound particles have a median value $a' \sim 0.70$, from which we calculate $e' \sim 0.76$. The actual median value is $e' \sim 0.85$ for the particles, which is $\sim$10 per cent larger than predicted. This is probably the result of the continued interaction of the primary and the captured particles as the perturber recedes from pericentre. The particle transfer does not occur in a well-defined stream, which results in a large spread in semimajor axes and eccentricities. However, the captured particles appear to manifest as an asymmetrical disc about the perturber (upper panel of Fig. 15), and show clustering in e' and a' (lower panel of Fig. 15), indicating some level of coherence in the transfer (seen in Fig. 4). Scaling according to KLSS, we find that 90 per cent of the disc particles are located within 500 au of the perturber. For the KLSS model (i.e. the previous model augmented with an orbital inclination of 30° for the perturber), the median eccentricity and semimajor axis are each found to be $\sim$0.7, consistent with the higher relative disc velocity expected for the inclined encounter.

The luminosity of an M0V dwarf star (of mass $\sim 0.5\,M_\odot$, corresponding to $\mu = 0.3$) is $\sim 10^2$ times smaller than for β Pic. If the amount of scattering surface in the disc is proportional to the square of the number of parent bodies (e.g. Backman & Paresce 1993), then as an upper limit the brightness of the perturber's disc is expected to be $\sim 10^4$ times fainter than that around β Pic, and $\sim 10^2$ times fainter relative to the central star. Thus it is plausible that the perturber may demonstrate a measurable scattered-light disc as a result of collisional erosion amongst the captured planetesimals at the distance to β Pic.

3.5 Close encounters with a bound perturber

Since the innermost mid-plane brightness feature identified by KLSS is measured to be at $\sim$500 au, the age of the rings in the β Pic disc should be $\sim 10^5$ yr, as calculated above. Although this figure could be revised up or down according to future observations, we shall take this to mean that the epoch of the fly-by encounter was about 10^5 yr in the past. Use of the *Hipparcos* survey data reveals that this is also the minimum time-scale we must look back from the present in order to find a perturber fly-by at $\lesssim 10^5$ au (Kalas et al. 2001). The 18 most closely approaching stars identified by Kalas et al. (2001) have a mean encounter velocity $\sim 40\,\mathrm{km\,s^{-1}}$, which is considerably higher than that deduced from our dynamical calculations. Thus we are prompted to consider companions that are or were physically associated with β Pic.

Repeated close encounters of the bound star with the disc may destroy the asymmetrical disc structure and ring features set up by the first encounter. Since for $e < 1$ the semimajor axis of the perturber can be written as $q/(1 - e)$, by demanding the orbital period to be greater than some value $P_{\min}$, we deduce

$$e > 1 - q\left[\frac{4\pi^2}{G(M_\mathrm{p} + M_\mathrm{s})P_{\min}^2}\right]^{1/3}. \qquad (9)$$

Thus if we take $P_{\min} = 10^5$ yr, we infer that the perturbed binary eccentricity needs to be greater than 0.75, in order that we may view the ring features at their inferred age.

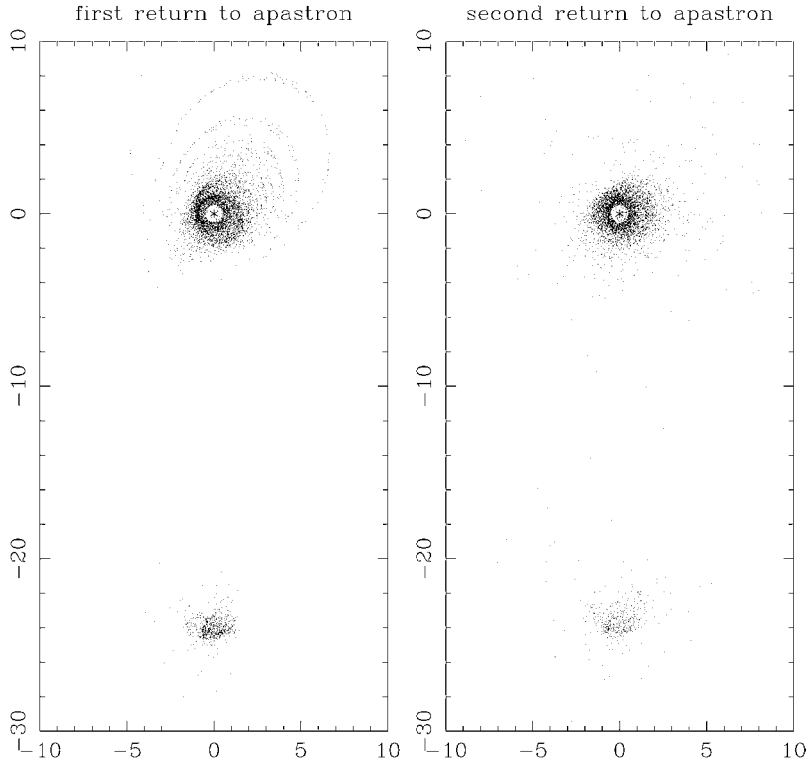

Figure 17. Particle positions corresponding to data given in Fig. 16. The position of the primary is plotted with an asterisk.

In Fig. 6 we show a trajectory with $e = 0.75$. The similarity of such high-eccentricity bound orbits to the parabolic trajectory suggests that the disc response should be similar. In Fig. 16 we give plots of the apocentre distance versus longitude of pericentre for a coplanar encounter simulation with $e = 0.8$, $\mu = 0.3$ and $q = 2.6$. The perturber starts at apocentre and we give results for the first and second completed orbital periods. Clearly the length asymmetry is completely disrupted after the second encounter. In Fig. 17 we give the corresponding particle positions, which show that the ring structure is also destroyed after the second encounter. Thus as suspected only a single fly-by can be allowed.

Possible scenarios in which a single pericentre passage could have occurred in the recent past are as follows: (1) The perturber was originally a bound companion to β Pic with a sufficiently large pericentre distance that no significant interaction with the disc occurred over its lifetime, and with sufficiently large semimajor axis and eccentricity that it could be perturbed into the required trajectory by the close fly-by of a massive field star $\sim 10^5$ yr in the past. (2) β Pic was a hierarchical multiple system that was dynamically unstable on a time-scale comparable to its present age, resulting in the ejection of one or more stars and the development of a disc-intercepting orbit for another, or an ejected star passed by β Pic on its way out of the system.

In the first scenario the three-body interaction should have occurred at least 10^5 yr ago. The further in the past we put this event, the more eccentric the resultant binary orbit must be in order to delay closest approach until 10^5 yr ago (if the perturbed star has an initially out-going trajectory). Although perhaps more attractive than the lower-probability close binary encounter model used by KLSS, the problem of low relative velocity is shifted from the star–disc interaction to the interaction between the second and third bodies. In respect of the second scenario we point out that Weinberger et al. (2000) report an age of 5 Myr for the triple system HD 141569. This consists of a Vega-like BVe primary with a 500 au disc and two M stars each at $\sim$1000 au projected separation. Weinberger et al. (2000) deduce that the relative separations involved may make the system unstable, giving the possibility that HD 141569 represents an earlier stage in the evolution of the β Pic system (with an age of 20 Myr). Studies of the dynamics involved suggest that young stars with multiple companions may not lose some of them via dynamical instability until main-sequence ages (Eggleton & Kiseleva 1995), which is supported by observations of high binary frequency amongst young stars compared to field stars (Mathieu 1994).

4 DISCUSSION

Here we have considered the stellar fly-by hypothesis that may account for the asymmetrical structure in the scattered-light dust disc of β Pic. We investigated the dynamics of the perturbed planetesimal disc in an attempt to learn more about the possible parameters of a fly-by encounter. Additionally, we have described the origin of transient circumstellar eccentric ring structures as being a general outcome of an encounter, resulting from the reflex motion of the primary star as the perturber passes through closest approach. The apparent ring system is actually an eccentric tightly wound one-armed spiral pattern that gradually disappears because of phase mixing in the particles' orbital motion. In inclined-orbit simulations we find that the vertical disc response also has analogues in the scattered-light disc of β Pic. We summarize the coplanar results in Fig. 18, and the inclined-orbit results in Fig. 19.

For the perturber we conclude that the mass should not be very different from $0.5\,M_\odot$ (corresponding to spectral type M0V). In this case we favour a low-inclination prograde encounter with relative velocity of a few km s^{-1}, which makes a bound perturber seem the most natural choice. One problem with this is that

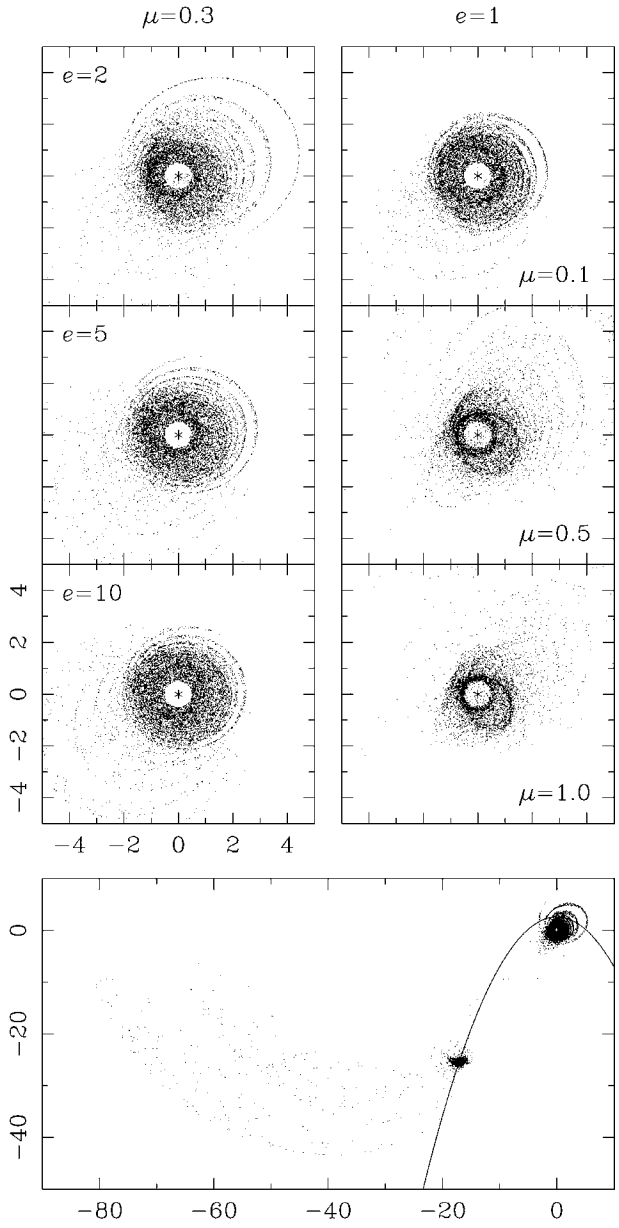

Figure 18. Summary of coplanar model results in face-on particle plots. The models were run for 120 time units, with the perturber initialized a radial distance of 20 units from the primary. After much longer times the phase mixing in the particles' orbits results in dissolution of the ring features, maintaining the distended envelopes of the discs seen above. The position of the primary is plotted with an asterisk. The top left-hand side panel shows results for models with $\mu = 0.3$ and from top to bottom $e = 2$, 5 and 10 respectively. The top right-hand side panel shows results for models with $e = 1$ and from top to bottom $\mu = 0.1$, 0.5 and 1 respectively. The bottom panel shows results, on a larger scale, for the model with $e = 1$ and $\mu = 0.3$. The perturber trajectory is shown with a solid line. We see: the perturbed disc with rings, the captured particles clustered about the instantaneous position of the perturber, and escaping particles (the large arcs on the left-hand side of the plot).

asymmetries would be destroyed in the second pericentre passage. Thus, given the deduced youth of the asymmetries, the perturber in this scenario is required to make a single close approach in the recent past (i.e. $\sim 10^5$ yr ago). This can be accounted for by making the perturber–β Pic system an initial wide binary that is perturbed by a massive passing field star $\sim 10^5$ yr in the past, such that the perturber is sent into a close approach orbit about β Pic. A more probable solution is to arrange for β Pic to have originally been a hierarchical multiple system (cf. HD 141569; Weinberger et al. 2000) that became dynamically unstable on the age of the star, and with the result being that one component was sent into a disc-intercepting orbit. In any case the perturber should have captured planetesimals from the primary's disc and may exhibit a detectable scattered-light disc as a result. A survey of a more extended field around β Pic than has been considered previously is in progress in order to test our hypotheses.

The dynamical response of the models suggests that the β Pic disc might be separable into different components corresponding to groupings of perturbed particle orbits. For example, we find that outwards of $\sim$250 au the SW extension may not have a distinct mid-plane owing to pumping of particle inclinations. The positions close to pericentre of the moderately eccentric NE mid-plane particles could account for the measurement of a SW mid-plane out to $\sim$650 au, in superposition with the more diffuse vertically and radially extended component. When the optical image is vertically compressed (Fig. 2) we are able to measure the SW extension to much larger radii (1450 au). In our model the corresponding (very eccentric and inclined) particle orbits also intersect the disc near to their pericentres (down to $\sim$50 au), possibly accounting for the inferred inner warp of the disc, which is aligned with the outer flared envelope in the SW. In summary, there are three recognizable particle groupings that can be related to the morphology of the β Pic disc. These are: the highly eccentric and inclined particles that reach apocentre in the SW (extension B particles); the moderately eccentric and weakly inclined particles that reach apocentre in the NE (extension A particles); and the relatively unperturbed particles inside $\sim$200 au radius (Figs 12 and 13).

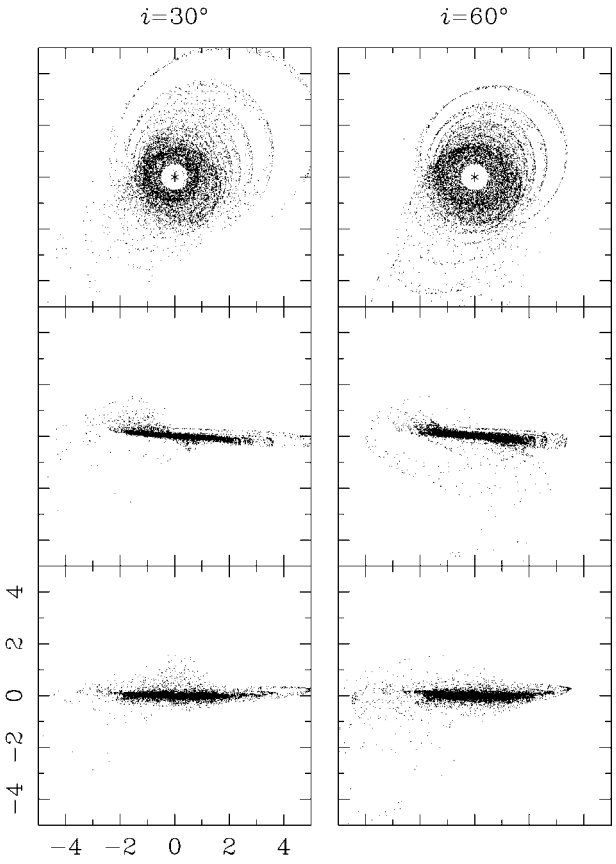

Figure 19. Summary of inclined-orbit models in face-on and edge-on particle plots. The models were run for 120 time units, with the perturber initialized a radial distance of 20 from the primary. The left-hand panel shows results for the model with $e = 1$, $\mu = 0.3$ and $i = 30°$. The right-hand panel shows results for the corresponding case with $i = 60°$. Uppermost frames are face-on views, middle frames are edge-on projections along the horizontal axis (line of nodes), and bottom frames are edge-on projections along the axis defining $i = 0$. Thus the projections are on to the three mutually orthogonal Cartesian planes of the computational coordinate system. The position of the primary is plotted with an asterisk.

ACKNOWLEDGMENTS

We are grateful to the University of Hawaii for supporting the observations. This work was funded in part by a grant from NASA held by D. Jewitt. We also thank J. Gradie, B. Zuckerman and E. Becklin for the use of their coronagraph. The clarity of this paper was improved by comments from S. Ida. Finally, P. Kalas acknowledges financial support and hospitality given by the Astronomy Unit, Queen Mary & Westfield College, during his visit there.

REFERENCES

Aumann H. H., 1988, AJ, 96, 1415
Backman D. E., Gillett F. C., 1987, in Linsky J. L., Stencel R. E., eds, Lecture Notes in Physics Vol. 291, Cool Stars, Stellar Systems and the Sun. Springer-Verlag, Berlin, p. 340
Backman D. E., Paresce F., 1993, in Levy E. H., Lunine J. I., eds, Protostars and Planets III. Univ. Arizona Press, Tucson, p. 1253
Burrows C. J., Krist J. E., Stapelfeldt K. R., 1995, BAAS, 187, 32
Clarke C. J., Pringle J. E., 1993, MNRAS, 261, 190
Eggleton P., Kiseleva L., 1995, ApJ, 455, 640
Frank J., King A., Raine D., 1992, Accretion Power in Astrophysics. Cambridge Univ. Press, Cambridge, p. 55
Hall S. M., Clarke C. J., Pringle J. E., 1996, MNRAS, 278, 303
Ida S., Larwood J., Burkert A., 2000, ApJ, 528, 351
Kalas P., Jewitt D., 1995, AJ, 110, 794
Kalas P., Larwood J., Smith B. A., Shultz A., 2000, ApJ, 530, L133 (KLSS)
Kalas P., Deltorn J. M., Larwood J., 2001, ApJ, in press (astro-ph/0101364)
Lin D. N. C., Papaloizou J. C. B., 1979, MNRAS, 186, 799
Mathieu R. D., 1994, ARA&A, 32, 465
Mouillet D., Larwood J. D., Papaloizou J. C. B., Lagrange A. M., 1997, MNRAS, 292, 896
Pfalzner S., Kley W., 2001, A&A, submitted
Press W. H., Teukolsky S. A., Vetterling W. T., Flannery B. P., 1992, Numerical Recipes in FORTRAN. Cambridge Univ. Press, Cambridge, p. 710
Smith B. A., Terrile R. J., 1984, Sci, 226, 1421
Smith B. A., Terrile R. J., 1987, BAAS, 19, 829
Toomre A., Toomre J., 1972, ApJ, 178, 623
Weidenschilling S. J., Cuzzi J. N., 1993, in Levy E. H., Lunine J. I., ed., Protostars and Planets III. Univ. Arizona Press, Tucson, p. 1031
Weinberger A. J., Rich R. M., Becklin E. E., Zuckerman B., Matthews K., 2000, ApJ, in press (astro-ph/0007170)
Whitmire D. P., Matese L. J., Tomley L. J., 1988, A&A, 203, L13

This paper has been typeset from a TEX/LATEX file prepared by the author.